ELSEVIER

Contents lists available at ScienceDirect

# Materials Chemistry and Physics

journal homepage: www.elsevier.com/locate/matchemphys





# Surface and defect engineered polar titanium dioxide nanotubes as an effective polysulfide host for high-performance Li-S batteries

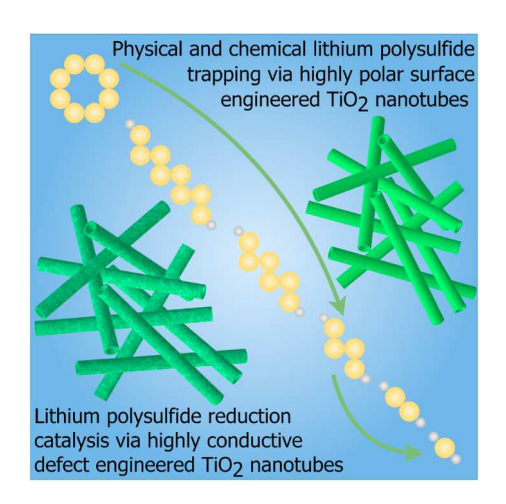
Zephyr Barlow, Zhen Wei, Ruigang Wang

Department of Metallurgical and Materials Engineering, The University of Alabama, Tuscaloosa, AL, 35487, United States

#### HIGHLIGHTS

- Surface and defect engineered TiO<sub>2</sub> nanotubes provide a high surface area polar host material for mitigating lithium polysulfide shuttling.
- Combination of physical confinement and chemical binding adsorption.
- Robust 3D hierarchical structure for mitigating the shuttle effect of lithium polysulfide.

#### GRAPHICAL ABSTRACT



# ARTICLE INFO

# Keywords: Lithium-sulfur battery High surface area polar materials High surface area catalysts Titanium dioxide nanotube Cathode polar host

# ABSTRACT

In this work, the surface structure of as received and ball milled (BM) titanium dioxide ( $TiO_2$ ) was modified via a simple hydrothermal method to create nanotubes ( $TiO_2$  NTs and  $TiO_2$  BM NTs) and subsequently chemically reduced to introduce widespread oxygen vacancy defects ( $TiO_{2-x}$  NTs and  $TiO_{2-x}$  BM NTs). The high surface area, innate polar nature, and high conductivity of  $TiO_2$  NTs allow the host material to effectively trap the lithium polysulfides both physically and chemically and improve the redox kinetics of lithium polysulfides. Chemical reduction acts to further improve the performance of the NTs by increasing the amount of polysulfides that can be adsorbed and by further increasing the conductivity of the material. Galvanostatic charge-discharge cycling testing revealed good performance for all four of the tested cathode hosts, with the best performance being achieved by  $TiO_2$  BM NTs and  $TiO_{2-x}$  NTs, with the former delivering an initial discharge capacity of 1204.72 mAh  $g^{-1}$  at 0.1 C and 767.69 mAh  $g^{-1}$  at 3 C and the latter delivering an initial discharge capacity of 1005.24 mAh  $g^{-1}$  at 0.1 C, 353.7 mAh  $g^{-1}$  at 3 C, and a decay rate of -0.68% per cycle over the first 300 cycles at 3 C.

E-mail address: rwang@eng.ua.edu (R. Wang).

 $<sup>^{\</sup>star}$  Corresponding author.

#### 1. Introduction

In order to address the ever-growing demand for clean and sustainable energy facing our world, novel energy storage devices and/or systems that have a low environmental impact at all stages of production and use, low cost, high cycle life, and that boast higher energy densities than existing solutions are necessary. Such energy storage devices and/ or systems would allow the development of longer-range electric vehicles and higher capacity batteries for mobile devices by virtue of their higher energy density and would lower the cost of high-volume energy storage for stabilizing output from renewable sources (i.e., solar or wind energy, etc.) by virtue of its lower cost and higher cycle life [1]. A prime candidate for this unfilled need is the lithium-sulfur (Li-S) battery, as it addresses all of these identified needs well. Li-S batteries boast a theoretical specific capacity of 1,675 mAh g<sup>-1</sup> and a theoretical energy density of 2,600 Wh kg<sup>-1</sup> [2–4], as compared to the theoretical specific capacity of 272 mAh g<sup>-1</sup> of current lithium-ion batteries [5], about six times greater. Additionally, the sulfur cathode has several promising attributes. The average price per metric ton of sulfur in 2022 stood at 150 USD, as compared to the 68,000 USD and 25,000 USD per metric ton of cobalt and nickel respectively [6]. Sulfur is also naturally abundant and boasts superior environmental compatibility [7,8].

The commercialization and further development of Li-S batteries are currently limited by several major issues, those being 1) the large change in volume of sulfur during its reduction, 2) the insulating nature and poor ionic conductivity of sulfur and lithium polysulfides  $(10^{-13} \text{ S})$ cm<sup>-1</sup> for Li<sub>2</sub>S), and 3) particularly the lithium polysulfide diffusion known as polysulfide shuttling effect (PSE), leading to low sulfur utilization and rapid capacity decay [9-11]. To overcome the technical obstructions mentioned above and promote the commercialization of Li-S batteries, various sulfur host or additive materials have been developed aiming to effectively encapsulate sulfur species and alleviate the severe shuttling issue of polysulfides. Carbon materials serving as efficient sulfur host materials have been extensively investigated due to their intrinsic high conductivity, cost-effectiveness, and outstanding structural tunability (1D, 2D, and 3D structures) [12]. However, only limited obstruction of polysulfide migration can be fulfilled by carbon host materials due to weak chemical affinity capability towards polysulfides, resulting in poor sulfur utilization, undesirable rate capability, and rapid capacity attenuation in long cycling battery tests [13].

Compared with the weak physical interaction of carbon-based sulfur host materials, metal-based polar compound materials can demonstrate strong chemical adsorption and immobilize polysulfides [14]. Metal sulfides, metal carbides, metal nitrides, and metal oxides have all been identified as viable polar host materials for Li-S batteries. Metal sulfides offer a polar interaction with lithium polysulfides, have demonstrated high catalytic abilities for lithium polysulfide reduction, and boast a high electrical conductivity compared to other metal-based compound hosts. Metal carbides demonstrate electrocatalytic abilities due to their high conductivity and transition metal carbides have been shown to demonstrate polar interactions with lithium polysulfides. Metal nitrides offer polar host interactions, high conductivity, and boast a stable structure. Metal oxides offer a strong polar interaction with lithium polysulfides due to the presence of oxygen anions in addition to metal cations, resulting in a large amount of active polar sites for adsorption [15].

Titanium dioxide ( $TiO_2$ ) has been used as polar host material due to its strong polysulfide adsorption capability, desirable polar surface along the (0 1 1) plane of rutile phase  $TiO_2$ , and chemical/electrochemical stability [16].  $TiO_2$  exhibits this high capacity to adsorb lithium polysulfides due to a strong chemical interaction between  $Ti^{4+}$  and lithium polysulfides and also has shown the ability to catalyze the lithium polysulfide reduction reaction [17]. Recently, numerous reports on various high surface area nanostructures of  $TiO_2$ , such as nanoparticles [16], nanowires [18], nanosheets [19], and nanofibers [20], have demonstrated that the soluble intermediate polysulfides can be

trapped successfully to alleviate the huge loss of active material sulfur induced by PSE. The properties which make  $TiO_2$  a suitable cathode host material for Li-S batteries can be further improved through its reduction via thermal or chemical processes to  $TiO_{2-x}$ . Reduced  $TiO_2$  ( $TiO_{2-x}$ ) boasts a higher electrical conductivity and a higher polysulfide adsorption capacity than pristine  $TiO_2$  owing to the higher concentration of surface oxygen vacancies which act as adsorption sites. The presence of a large number of oxygen vacancies in the  $TiO_{2-x}$  material also causes it to demonstrate catalytic properties due to the presence of titanium ions with lower oxidation states such as  $Ti^{3+}$  which further increase electron mobility and serve to lower the activation energy needed to initiate the lithium polysulfide reduction reaction [21,22].

Many different nanostructures and forms of TiO2 have already been investigated and have shown promising results. For example, Huang et al. [23] reported that hierarchically porous titanium dioxide showed excellent performance as both a polar host and as a physical immobilizer for lithium polysulfides. Nanoscopic pores in the host material demonstrated a superior ability to physically confine lithium polysulfides, and the very high surface area of 235.6 m<sup>2</sup> g<sup>-1</sup> greatly increased the area on which polar interactions can occur. This strategy produced excellent results, able to provide a specific capacity of 786 mAh g<sup>-1</sup> after 500 cycles at a charging rate of 2 C, and a maximum initial specific capacity of 1186 mAh g<sup>-1</sup> at 0.1 C. Cai et al. [24] reported that TiO<sub>2</sub> nanowire clots have also been employed as a sulfur host material due to their very high surface area to volume ratio of 270.1  $\text{m}^2\text{ g}^{-1}$ . The high surface area of the polar host material provides more possible locations or adsorption sites for the lithium polysulfides to form polar bonds with TiO<sub>2</sub>, boasting retention. This method was able to provide a specific capacity of 404.5 mAh g<sup>-1</sup> after 200 cycles at 2 C and boasted a maximum initial specific capacity of 1163 mAh g<sup>-1</sup> at 0.1 C. Park et al. [25] reported that hollow sulfur-carbon nanospheres with a layer of polar TiO2 were used to physically and chemically confine lithium polysulfides via polar bonds and complicated geometry. This method provided a specific capacity of 630 mAh g<sup>-1</sup> after 500 cycles at 1 C and a maximum initial specific capacity of 1239 mAh g<sup>-1</sup> at 0.1 C. Liu et al. [26] reported that hierarchically porous TiO<sub>2-x</sub>/carbon hybrid nanofibers enabled the creation of Li-S cells with high sulfur loading and utilization that demonstrated excellent rate performance and high cycling stability. The combination of the high surface area of the polar host material and the catalytic properties of the Ti<sup>3+</sup> ions present from the oxygen deficiency enabled impressive cell performance, with cells using the material demonstrating an initial specific capacity of  $1360 \text{ m}^2 \text{ g}^{-1}$  at a rate of 0.5 C, with a specific capacity 780 m $^2$  g $^{-1}$  maintained after 500 cycles.

According to the previously published work,  $TiO_2$  nanotubes (NTs) have a specific surface area of 233.8 m<sup>2</sup> g<sup>-1</sup> [27] and an electronic conductivity of  $1\times 10^{-7}$  S cm<sup>-1</sup> [28]. They are generally prepared via complicated procedures with multiple variables such as the anodization and electrodeposition method [29], the dealloying method [30], or the template method [31,32]. These procedures greatly increase the cost of production and hinder the large-scale commercialization of the final material. It is well acknowledged that the simple and cost-effective hydrothermal method is of great promise for the preparation of  $TiO_2$  NTs.

The hydrothermal technique is one of the most frequently used methods for the synthesis of various well-dispersed and "homogeneous" nanomaterials. All the reactants are dissolved in an autoclave with a suitable solvent under high pressure and low-temperature ( $<250\,^{\circ}$ C) conditions depending on the desired composition, crystal structure, size, and shape of the nanomaterials. The main advantage of hydrothermal technique is that the hydrothermal method can produce nanomaterials with high vapor pressures and controllable exposed crystal facets (i.e., different morphologies). In addition, via liquid phase or multiphase chemical reactions, the compositions of nanomaterials to be synthesized can be precisely regulated in the hydrothermal system.

In this report, surface and defect engineered  $TiO_2$  NTs are synthesized via a hydrothermal template method from two different precursor materials and subsequently chemically etched to introduce oxygen

vacancies. These four cathode host materials,  ${\rm TiO_2}$  NTs,  ${\rm TiO_2}$  ball mill (BM) NTs,  ${\rm TiO_{2-x}}$  NTs, and  ${\rm TiO_{2-x}}$  BM NTs respectively, were analyzed to determine the impact of initial particle size on the growth and mechanical robustness of NTs, and to determine the effects of surface and morphology engineering on the performance of  ${\rm TiO_2}$  NTs based materials as cathode hosts for Li-S batteries. Each sample is also chemically etched to determine the impact of widespread oxygen vacancies (defect engineering) on the conductivity of the material and cell performance.

# 2. Experimental section

# 2.1. Preparation of TiO2 nanotubes

TiO2 NTs were created through a modified one-step hydrothermal template synthesis method using rutile  $TiO_2$  powder [33]. A titanium dioxide/sodium hydroxide solution was created by adding 2 g rutile TiO<sub>2</sub> powder (predominantly rutile titanium (IV) oxide, 99.999%, Acros Organics) to 80 mL 10 M NaOH (prepared from ACS sodium hydroxide pellets). This solution was then stirred vigorously for 24 h to ensure total dissolution of the TiO2. This solution was then added to a 200 mL Teflon autoclave and sealed. Hydrothermal synthesis was performed in a programable box furnace at 150 °C with a hold time of 72 h. After the furnace was allowed to cool to ambient temperature, the autoclave was removed and unsealed. The contents of the autoclave were poured into a vacuum filtration system, with the deposited TiO2 NT being scraped out of the autoclave and put in the filter. The nanotubes were then washed with 40 mL 0.1 M HCl to neutralize and eliminate the remaining sodium ions and 500 mL deionized water to dissolve ions left on the TiO2 NTs. Once filtration was complete, the filter paper was removed from the vacuum filtration system and put in a vacuum oven where it was dried for 24 h at 80 °C. This process was performed twice, once using the rutile TiO<sub>2</sub> powder as it was received to create TiO<sub>2</sub> NTs, and once using rutile TiO<sub>2</sub> powder that had been ball milled (TiO<sub>2</sub> BM) to reduce the particle size to create TiO<sub>2</sub> BM NTs. The latter sample was prepared to assess the impact of initial particle size on the morphology of NTs synthesized via the template method.

# 2.2. Preparation of TiO<sub>2-x</sub> nanotubes

 ${\rm TiO_{2\cdot x}}$  NTs were prepared via a simple chemical etching procedure [3,34].  ${\rm TiO_2}$  NT powder was dispersed in DI water via magnetic stirring in a 250 mL beaker to create a suspension. 10 wt percent (10 wt%) NaBH<sub>4</sub> (relative to the weight of  ${\rm TiO_2}$  NTs) was then added to the suspension. This mixture was then vigorously stirred for 12 h via a magnetic stirrer. The sample was then filtered and dried in a vacuum furnace for 12 h to obtain  ${\rm TiO_{2\cdot x}}$  NTs. This exact procedure was performed using  ${\rm TiO_2}$  BM NT to create  ${\rm TiO_{2\cdot x}}$  BM NT for analysis and comparison.

# 2.3. Preparation of electrolyte solution and Li<sub>2</sub>S<sub>6</sub> catholyte solution

The electrolyte solution was prepared by combining dioxolane and dimethoxyethane (DOL: DME) (Alfa Aesar, 99%) in a 1:1 volume ratio, and adding lithium bis(trifluoromethane) sulfonimide (LiTFSI) (AdipoGen Life Sciences, 99%) and LiNO $_3$  (Alfa Aesar, 99.999%) to create a solution containing 1 M LiTFSI and 0.5 M LiNO $_3$ . In this solution the DOL:DME acts as a solvent for lithium ions and lithium polysulfides and the LiTFSI and LiNO $_3$  act as initial sources of lithium ions. Specifically, 2 mL DOL and 2 mL DME were combined with 1.15 g LiTFSI and 0.15 g LiNO $_3$ . The solution was then stirred vigorously for 24 h in a sealed container. The resulting solution was clear and had no apparent sedimentation.

The  $\text{Li}_2S_6$  catholyte solution was prepared by combining the prepared electrolyte solution with  $\text{Li}_2S$  (Alfa Aesar, 99.9%) and sublimed elemental sulfur powder (Alfa Aesar, 99.5%) to create a 1.0 M  $\text{Li}_2S_6$  solution. Liquid  $\text{Li}_2S_6$  is used as the cathodic material in the cell in place of solid sulfur because its liquid phase allows it to be adsorbed and fully

permeate the host material instead of staying on its surface. This helps to stabilize the cell by preventing quick diffusion from the cathode surface to the anode surface. Specifically, 2 mL of the prepared electrolyte solution was combined with 92 mg Li $_2$ S (0.002 mol) and 320 mg sulfur powder (0.01 mol). The solution was then stirred vigorously at 60  $^{\circ}$ C for 24 h in a sealed container to facilitate the formation of Li $_2$ S $_6$  via the reaction:

$$Li_2S + 5S = Li_2S_6$$

The resulting solution was a deep reddish brown and had no apparent sedimentation.

# 2.4. Polysulfide adsorption test

A polysulfide adsorption test was performed on the  $TiO_2$ -derived cathode host materials to validate their potential to adsorb liquid lithium polysulfides from the solution. A 0.0033 M  $Li_2S_6$  (0.02 M S) solution was created by combining 4 mL of the prepared electrolyte solution with 13.36  $\mu$ L of the prepared catholyte solution. The polysulfide test solution was a dark yellow color, with no apparent sedimentation. For the control, 10 mg of very finely cut carbon cloth (Fuel cell earth, thickness = 0.381 mm, density = 1.75 g/cm³) was added to one vial and pushed to the bottom of the vial to ensure the entire sample was submerged and sealed. 10 mg of each host powder was then added to the other vials. 320  $\mu$ L of the 0.0033 M  $Li_2S_6$  solution was quickly added to each vial and each vial was sealed. An additional vial that had been left free of host powder was also filled with the test solution to act as a color reference. Images were recorded every 10 min until the test solutions were clear.

# 2.5. The TiO2 on carbon cloth electrode preparation

The TiO2 on carbon cloth electrodes were prepared by applying a slurry of each TiO2 derived host material to 15 mm discs which had been cut from carbon cloth (Fuel cell earth, thickness = 0.381 mm, density = 1.75 g/cm<sup>3</sup>) using a precision disc cutter. The host slurries were created by combining the host powder, super P carbon black (Alfa Aesar, 99%), and polyvinylidene fluoride (PVDF) at a 6.67:1:1 mass ratio in N-methyl-2-pyrrolixone (NMP) solvent. In this slurry, the TiO2 derived powder acts as the polar host material and catalyst, the super P carbon black acts to boost electrical conductivity, the PVDF acts as thermosetting polymer binder to anchor the other materials to the carbon cloth, and the NMP is a solvent able to effectively dissolve the powders to form a slurry. Specifically, 50 mg of the cathode host material, 7.5 mg super P carbon black, and 7.5 mg PVDF were combined with  $600\,\mu L$  NMP and stirred for 24 h in a sealed container. Once the slurry had been prepared, it was applied to the carbon cloth disc via a micropipette. Testing found that a deposited mass of between 2.0 and 3.0 mg of TiO2 NT host material showed ideal results. This was achieved by adding 30 µL of the slurry to the carbon cloth discs. Once the slurry had been applied, the cathode hosts were dried in a vacuum furnace at 60 °C or 24 h. The electrodes were obtained after vacuum drying. This process was repeated with each host material to create TiO2 NTs@CC, TiO2 BM NTs@CC, TiO2-x NTs@CC, and TiO<sub>2-x</sub> BM NTs@CC respectively.

# 2.6. Cell assembly

CR2032 coin-type cells were prepared in an argon-filled glove box by combining the previously synthesized materials with commercially available stainless steel battery casings, spacers, springs, and separator material. Cells were assembled by placing an electrode into a positive case and centering it. 10  $\mu L$  of the catholyte solution (corresponding sulfur loading = 1.085 mg/cm²) was then applied to the center of the loaded carbon cloth cathode, followed by 30  $\mu L$  of the electrolyte solution. A 19 mm disc of separator material, specifically Celgard 2500, was then placed on top of the loaded carbon cloth cathode to electronically

separate the cathode and anode side of the battery. 30  $\mu$ L of the electrolyte solution was added on top of the separator. A lithium metal anode disc was then placed on top of the separator, flat side down. A stainless-steel spacer and spring were then placed on top of the lithium metal anode, followed by the negative case. The cells were then crimped closed using 100 kg/cm<sup>2</sup> of force via a manual hydraulic press.

#### 2.7. Electrochemical testing

Galvanostatic charge/discharge cycling, cyclic voltammetry (CV), and electrochemical impedance spectroscopy (EIS) were then performed on completed cells at ambient temperature (at 25  $^{\circ}$ C). Galvanostatic charge/discharge cycling was performed on an MTI battery tester using a voltage window of 1.7–2.8 V and current densities ranging from 0.1 to 3 C (1C = 1675 mAh g $^{-1}$ ). CV measurements were taken with a Gamry Interface 1000 E Potentiostat/Galvanostat/ZRA instrument using a voltage potential window of 1.7–2.8 V and a scan rate of 0.1 mV/s. EIS measurements were taken using the same instrument, with a frequency window of 0.01–10 $^{5}$  Hz.

#### 2.8. Materials characterization

Powder X-ray diffraction (XRD) was performed using a Philips X'Pert MRP equipped with Cu K $\alpha$  source (wavelength  $\lambda = 0.154$  nm) at 45 kV and 40 mA on a finely ground powder sample of the nanotube material to characterize the overall crystal structure of the material and to match and compare it to database values. A scan speed of 0.06°/min was used to collect the XRD results ( $2\Theta$  range =  $10-90^{\circ}$ ). Scanning electron microscopy (SEM) was performed using an Apreo FE-SEM to assess the surface morphology of the nanotubes, and to gain insight on qualities such as porosity and distribution of nanostructures across the particles. Transmission electron microscopy (TEM) was performed using an FEI Tecnai F-20 TEM in order to analyze the interior structure of the nanostructures and validate the TiO2 NT was hollow. TEM samples were prepared by ultrasonicating finely ground TiO2 NT samples in a small amount of ethanol. After about 15 min of ultrasonication, a white suspension of TiO2 NT in ethanol was created. A single drop of this suspension was applied to a 400-mesh copper grid with an ultrathin carbon film (Ted Pella Inc.), and the sample was placed in a fume hood to dry until ready for TEM analysis. EDAX was performed using integrated equipment in the Apreo FE-SEM in order to assess material chemistry and the distribution of chemical elements within the structure.

# 3. Results and discussion

# 3.1. Characterization before cycling

Fig. 1 shows XRD data recorded for precursors and host materials to assess chemical and structural similarities. Fig. 1 (a and d) show data recorded for as received rutile TiO2 and ball milled rutile TiO2. The typical dominant peaks of rutile TiO<sub>2</sub> are located at 27.51°, 36.16°, 41.34°, 54.46°, 56.78° and 69.20°, representing the (1 1 0), (1 0 1), (1 1 1), (211), (220), and (301) planes respectively. This indicates that the ball milling procedure has only impacted the morphology of the precursor material and has not impacted structural or chemical characteristics. Fig. 1 (b) and e show data recorded for nanotubes synthesized via the hydrothermal template method with as received and ball-milled precursors respectively. XRD analysis indicated a mixed phase, comprised of rutile and anatase TiO<sub>2</sub> phases. The most dominant peaks recorded for both samples were located at 27.51°, 36.16°, 54.46°, and 69.20°, representing the (1 1 0), (1 0 1), (2 1 1), and (3 0 1) planes of the rutile phase and at  $25.50^{\circ}$ ,  $38.16^{\circ}$ ,  $48.40^{\circ}$ , and  $63.25^{\circ}$ , representing the (1 0 1), (0 0 4), (2 0 0), and (2 0 4) planes of the anatase phase. This mixed phase composition is supported by previous work which synthesized TiO<sub>2</sub> NTs via a hydrothermal method [35,36]. The mixed phase XRD reading stems from the fact that TiO2 NTs are anatase phases,

grown on the surface of a rutile phase precursor [37]. Fig. 1 (c and f) show data recorded for chemically reduced  ${\rm TiO_2~NTs}$  and  ${\rm TiO_2~BM~NTs}$ . The dominant peaks recorded for these samples were the same as those recorded for  ${\rm TiO_2~NTs}$  and  ${\rm TiO_2~BM~NTs}$ , however there were several disparities in peak intensity between the two samples. For example, the peak of the (2 1 1) rutile plane is much less intense in Fig. 1 (f) than in Fig. 1 (c). This could be due to the smaller particle size of the BM-derived NT samples producing a more fragile structure. This can be assessed using SEM imaging of each of the samples. The crystalline size estimation by XRD is provided in the supporting information (Table S1).

The difference in morphology between the TiO2 NTs and TiO2 BM NTs can quickly be assessed by comparing Fig. 2 (a and c) respectively. The larger initial particle size of the TiO2 NT sample causes the NTs to form as a sort of "mat" on the surface of the particle, where nanotubes are dispersed in a regular density at irregular orientations. The topography of the TiO2 NTs is dense and uniform with NTs layered on top of one another, causing a widespread porosity due to the gaps between the layered NTs. The smaller initial particle size of the TiO<sub>2</sub> BM NTs results in a significantly different topography. Rather than growing on the surface of the particles, the NTs grew between the smaller particles, forming a sort of "web" between particles of TiO2 which links them together and forms larger particles. The pores of the TiO<sub>2</sub> BM NT sample are much larger, as they are gaps between the NT linked BM particles rather than gaps between layered NTs. This results in much deeper porosity, though at a larger scale. Fig. 2 (b and d) correspond with TiO<sub>2-x</sub> NTs and TiO2-x BM NTs respectively. These images were captured at 35,000x rather than 50,000x due to severe charging issues with the materials making them difficult to image at high magnifications. TiO2-x NTs have a similar appearance to TiO<sub>2</sub> NTs, with a widescale mat of NTs still visible. The NTs in the TiO2-x NTs sample are significantly damaged from the chemical etching process; however, they are widely visible across the surface of the particles. The more fragile NTs of the TiO<sub>2-x</sub> BM NTs sample cannot be identified in the SEM imaging, and likely have been destroyed by the chemical etching. The NT "web" of the TiO<sub>2-x</sub> BM NTs has much less support than the NT "mat" of the TiO<sub>2-x</sub> NTs, resulting in it being a much less robust material. The resulting material is still extremely high surface area due to the deep pores between the small, linked particles.

In order to confirm the presence of hollow nanotubes in the  ${\rm TiO_2~NT}$  sample and to characterize the crystal structure of the material, TEM imaging and analysis were performed (Fig. 3 (a-c)). A regular TEM image (Fig. 3 (a)) was first obtained to demonstrate the interior structure of the nanostructures. As TEM shows the "shadow" of matter, the darker portions can be interpreted to be thicker (mass-thickness contrast mechanism), and thus interpreted as the walls of a hollow structure.

After this had been validated, high-resolution TEM images (Fig. 3 (b-c)) were taken to examine the crystalline planar spacing and an average tube diameter of the  ${\rm TiO_2}$  NT after grinding and ultrasonication to isolate individual structures. The analysis yields a result of a plane spacing of roughly 0.74 nm along the (2 0 0) plane, consistent with the results from other work which synthesized  ${\rm TiO_2}$  NTs via similar hydrothermal methods [38]. The TEM images were then analyzed to determine the diameter of the  ${\rm TiO_2}$  NTs. Analysis from different points on the structure yielded an average of about 11.2 nm, with values being clustered between 12 nm and 10 nm. A length could not be determined for the  ${\rm TiO_2}$  NTs, as the structures had to be pulverized and ultrasonicated in order to disperse them thinly enough to analyze single structures via TEM.

# 3.2. $Li_2S_6$ adsorption test

A polysulfide adsorption test was conducted to assess the chemical affinity capability of the synthesized  $\text{TiO}_2$  NT as a host. Two tests were conducted, one analyzing the carbon cloth host material and the other analyzing the  $\text{TiO}_2$  NT powder. The carbon cloth test acted as a control, to assess whether the adsorption of the lithium polysulfides was due to

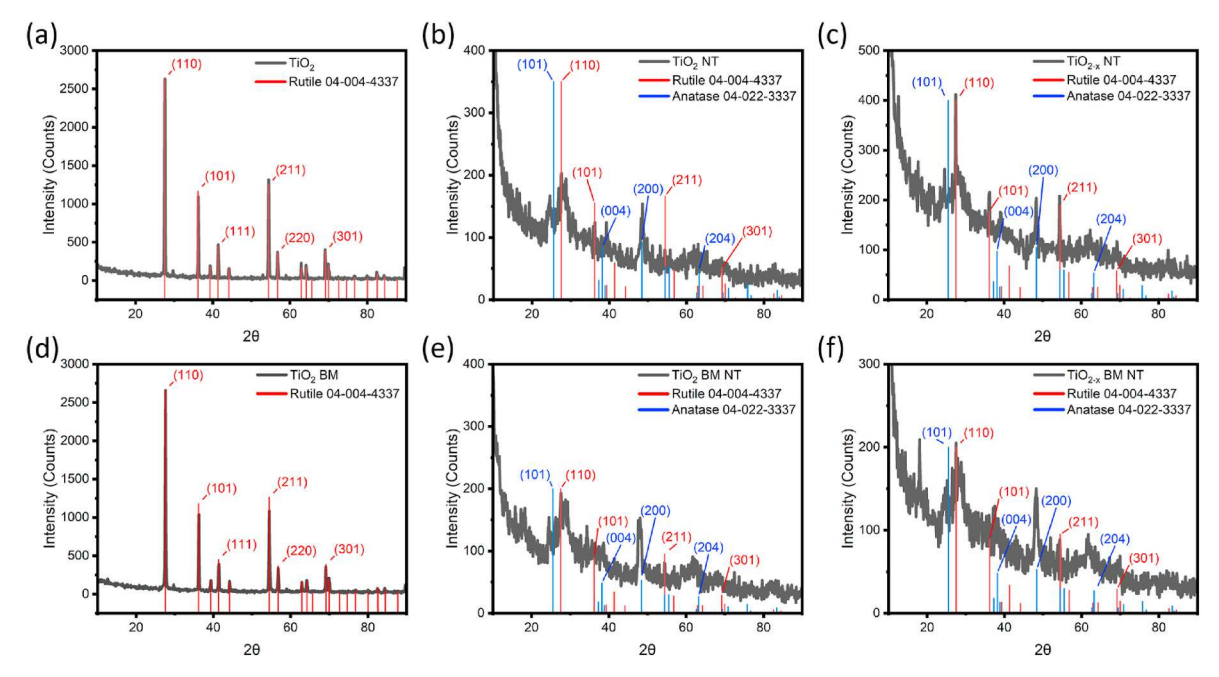


Fig. 1. XRD data obtained from each powder sample. Fig. 1 (a–c) show data for NTs synthesized using as-received  $TiO_2$  powder whereas Fig. 1 (d–f) show data for NTs synthesized using BM  $TiO_2$ . Fig. 1 a and d show XRD peaks for  $TiO_2$  and  $TiO_2$  BM, demonstrating that the low energy ball milling procedure has not changed the structure of the material in any way, only reduced the size of the particles. Fig. 1 b and e show the XRD peaks for  $TiO_2$  NTs and  $TiO_2$  BM NTs. Fig. 1 c and f show the XRD peaks for  $TiO_2$  NTs and  $TiO_2$  BM NTs.

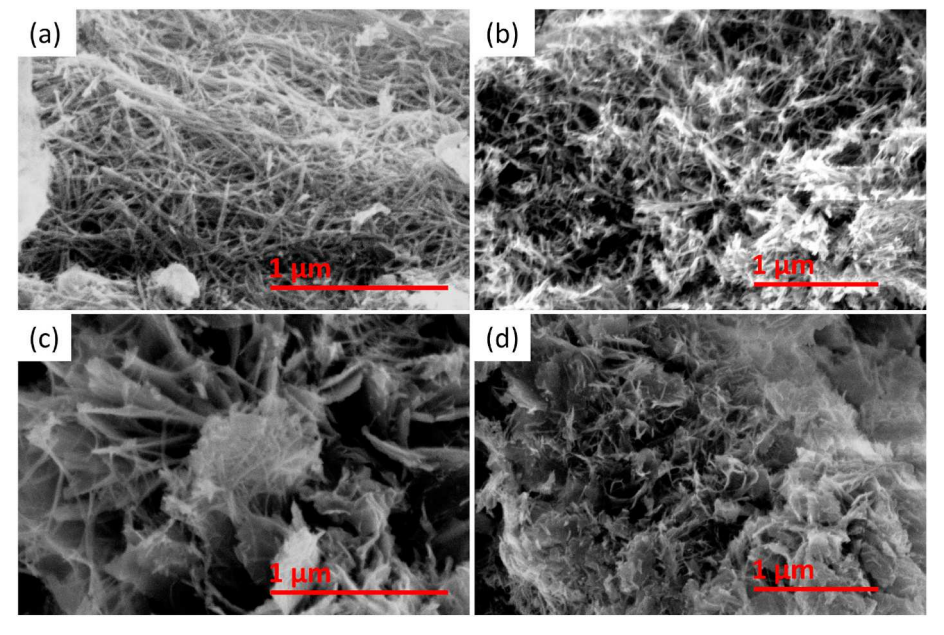


Fig. 2. SEM images of: (a): TiO<sub>2</sub> NTs, (b): TiO<sub>2-x</sub> NTs, (c): TiO<sub>2</sub> BM NTs and (d): TiO<sub>2-x</sub> BM NTs. Fig. 2 a and c were captured at 50,000x magnification while Fig. 2 b and d were captured at 35,000x magnification.

the  $TiO_2\ NT$  or due to the carbon cloth.

The adsorption test (Fig. 4 (a and b)) showed favorable results for the adsorption of liquid  $\text{Li}_2S_6$  lithium polysulfide.  $\text{Li}_2S_6$  was chosen for the adsorption test as it is the liquid phase lithium polysulfide present in the catholyte solution and one of the species vulnerable to PSE. The 0.0033 M  $\text{Li}_2S_6$  solution achieved a high level of adsorption in some samples, indicated by the change in intensity of the yellow coloration experienced over time. Adsorption is measured visually by referencing columns a) and b) of Fig. 4 (a), as these columns show the test solution with no host material and the carbon cloth used as an electrode and support structure

for the polar materials respectively. As evidenced by column b) of Fig. 4 (a), the carbon cloth electrode has no adsorptive capability, owing to the fact that carbon is a non-polar material. As shown in columns c) and d) of Fig. 4 (a), the raw materials,  ${\rm TiO_2}$  and  ${\rm TiO_2}$  BM respectively, demonstrate very little capability to adsorb the liquid polysulfides, indicating that any adsorptive capability of the material is due to the presence of nanotubes.

Columns e) and f) of Fig. 4 (a) show adsorption tests for  $TiO_2$  NTs and  $TiO_2$  BM NTs respectively and indicate that  $TiO_2$  NTs demonstrate a superior adsorptive capability than their ball-milled counterparts. This

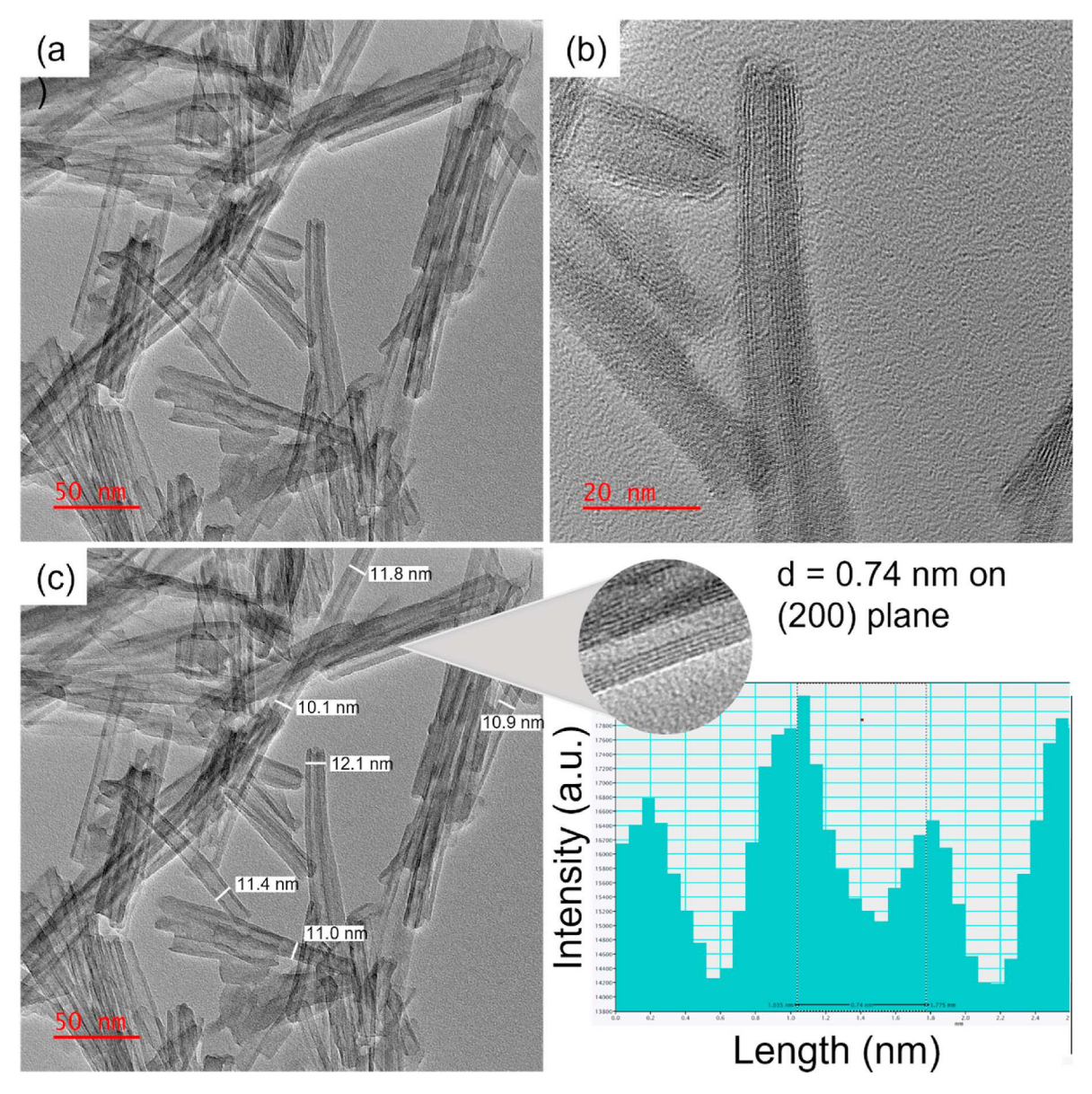
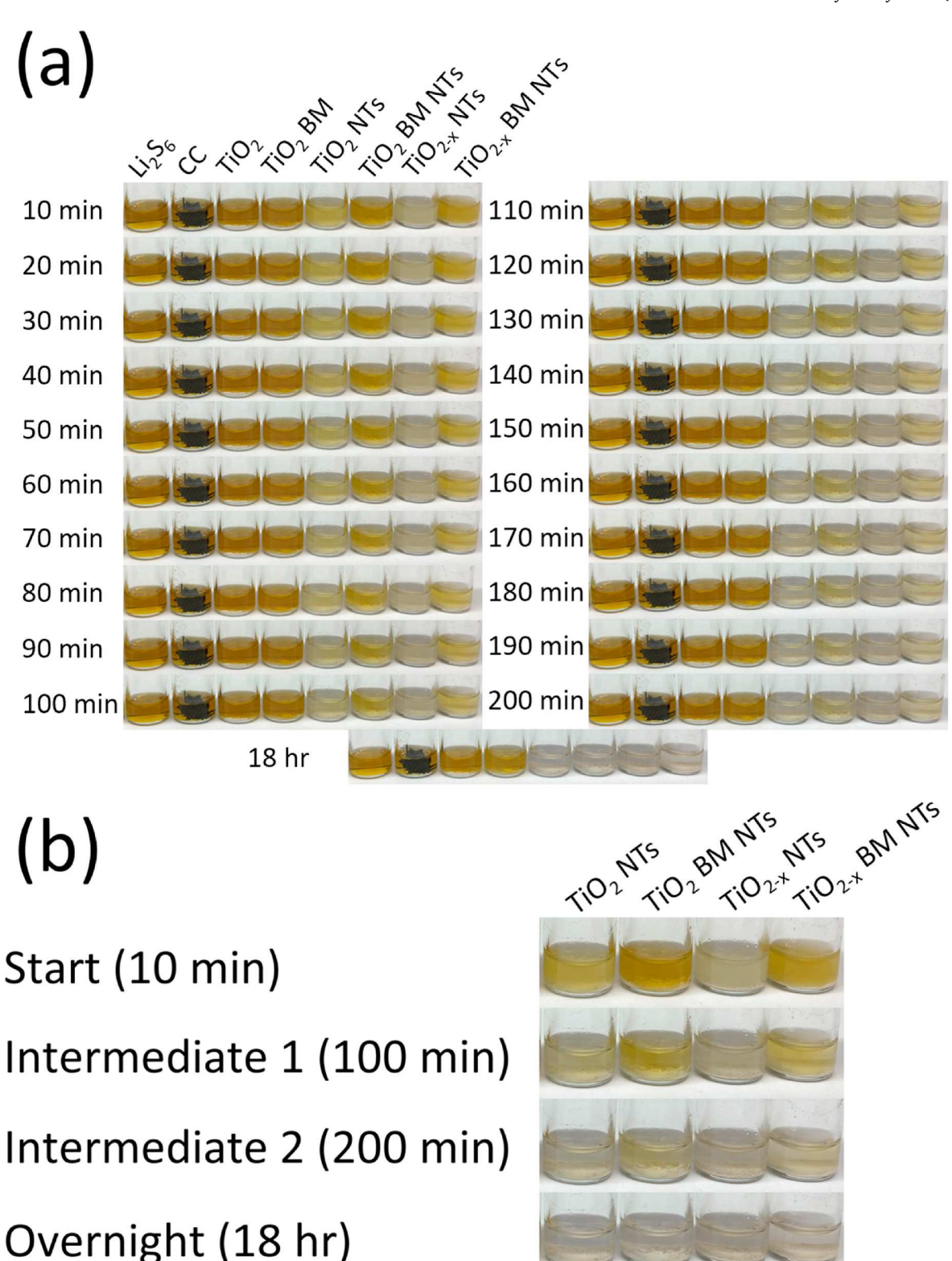


Fig. 3. (a) TEM image of TiO2 NTs. (b-c) High-resolution TEM images and the analysis of the diameter and the plane spacing of TiO2 NTs.

is indicated by the fact that the test conducted using TiO2 NTs was able to fully adsorb the Li<sub>2</sub>S<sub>6</sub> after about 190 min, whereas the test conducted using TiO2 BM NTs was not visibly clear until the next morning. Columns g) and h) of Fig. 4 (a) show adsorption tests for TiO<sub>2-x</sub> NTs and TiO<sub>2-x</sub> BM NTs respectively. The test conducted using the TiO2-x NTs noticeably changed color immediately after the introduction of the test solution, achieving full clarity after less than 1 h. The test conducted using TiO<sub>2-x</sub> BM NTs did not demonstrate the same performance, however it did demonstrate a slightly superior performance than the test using TiO2 BM NTs. Columns e), f), g) and h) are displayed at various intervals to show the shifts in the color of the solution more clearly in Fig. 4 (b). Two clear trends are observed in these images, firstly, that TiO2 NTs based host materials outperform the TiO<sub>2</sub> BM NTs samples significantly in terms of the speed of liquid polysulfide adsorption in both reduced and unreduced cases and secondly, that the reduced host materials outperform the unreduced host materials in both cases. The TiO2-x NTs sample demonstrated the best overall performance owing to several factors. Firstly, the highly robust high surface area material is able to accommodate a high level of adsorption. This is due to the higher presence of nanotubes than the TiO2 BM NTs based samples increasing the overall

available surface area for lithium polysulfides to be adsorbed on. Secondly, the TiO2 NTs are able to withstand chemical reduction to TiO2-x NTs, unlike the TiO2 BM NTs, allowing their adsorptive properties to be further boosted over the unreduced material. All four samples showed near total adsorption after being left overnight. These results suggest that the TiO2 NT based materials should all be suitable cathode host materials, as they are able to rapidly adsorb large amounts of soluble lithium polysulfides, helping to prevent the diffusion of polysulfides and the subsequent shuttling effect by "trapping" the sulfur species as soon as they dissolve into the electrolyte during the reduction reaction [39]. This is due to the aforementioned chemical affinity between Ti<sup>4+</sup> and lithium polysulfides, giving TiO2 a superior adsorption capability than other metal oxide hosts which rely on the affinity between oxygen and lithium polysulfides for adsorption [17]. This test also demonstrates that the TiO2 NTs outperform the TiO2 BM NTs in both unreduced and reduced states, indicating that their more robust geometry from the larger initial particle size allows them to better adsorb liquid polysulfides. The excellent performance of the TiO2-x NTs sample is likely due to a combination of the robust geometry of the material and the high presence of adsorptive Ti<sup>3+</sup> ion sites from chemical reduction.



**Fig. 4.** (a) Images taken at 10-min intervals displaying a polysulfide adsorption test for TiO<sub>2</sub> derived host materials. Column a) shows the test solution for reference, b) shows carbon cloth, c) shows TiO<sub>2</sub>, d) shows TiO<sub>2</sub> BM, e) shows TiO<sub>2</sub> NT, f) shows TiO<sub>2</sub> BM NT, g) shows TiO<sub>2-x</sub> NT, and h) shows TiO<sub>2-x</sub> BM NT. **(b)** images taken at various intervals for TiO<sub>2</sub> NT, TiO<sub>2</sub> BM NT, TiO<sub>2-x</sub> NT, and TiO<sub>2-x</sub> BM NT respectively for comparison.

#### 3.3. Electrochemical characterization

In order to quantify the electrochemical performance and assess the redox kinetics of each of the  $\rm TiO_2$  NT based cathode host materials, CR-2032 coin cells with an aerial sulfur loading of 1.085 mg/cm<sup>2</sup> were

created. EIS with a frequency window of  $0.01-10^5$  Hz was conducted to explore the kinetics of the Li-S electrochemical reaction and determine the internal impedance of the cell. Warmup cycling is performed to fully activate the cathodic material and allow the cell to reach its electrochemical equilibrium before analysis begins, allowing for a more

accurate reading to be obtained. The results of EIS testing are subsequently analyzed via the creation of a Nyquist plot to determine the internal resistances of the cells. The Nyquist plot is obtained by graphing  $Z_{real}\left(Z'\right)$  against the negative of  $Z_{imaginary}\left(Z''\right)$  and can be divided into three distinct regions, each indicating a different property of the cell. The first semicircle is in the high frequency region and indicates the interfacial (SEI: solid electrolyte interphase) resistance. The second semicircle is in the intermediate frequency region and indicates the charge transfer resistance. The third is the positive sloping line which falls in the low frequency region and indicates the Warburg impedance (W<sub>0</sub>), resistance which can be attributed to the diffusion of lithium ions in the electrolyte. Resistance values are obtained from the three inflection points on the Nyquist plot, with the electrolyte resistance (R<sub>s</sub>) being found from the initial value, SEI resistance (Rf) being found from the inflection point after the first semicircle, and charge transfer resistance (R<sub>ct</sub>) being found from the inflection point after the second semicircle [40]. The results of this testing are shown in Fig. 5 (a and b), and the equivalent circuit is shown in Fig. 5 (c).

As demonstrated by Fig. 5 (b), all cells demonstrated impressively low internal resistances.  $R_{s}$  values for each cell type were similar, owing to the fact that all cells used identical electrolyte solutions and were constructed in a nearly identical fashion.  $R_{f}$  values differed some, with the cell employing a TiO $_{2}$  NTs@CC cathode demonstrating a significantly lower resistance due to SEI. This can be attributed to the higher surface area of the TiO $_{2}$  NTs material than the other three TiO $_{2}$  based hosts, as this cathode is able to "spread out" the SEI and reduce the impact at any one point.  $R_{ct}$  values varied significantly, with the TiO $_{2}$ 

NTs@CC cathode demonstrating the worst performance. The  $TiO_{2-x}$  NTs@CC and  $TiO_{2-x}$  BM NTs@CC cathode demonstrated impressively low resistance to charge transfer, owing to their increased conductivity from the introduction of oxygen vacancies via chemical reduction. The  $TiO_2$  BM NTs@CC cathode demonstrated the best charge transfer performance of the samples, potentially owing to its high surface area or an unidentified factor related to the ball milling process.

Similarly, CV measurement with a potential window of 1.7-2.8~V and a scan rate of 0.1~mV/s was conducted to analyze the impact of the various cathode host materials on cell performance. Fig. 5 (d) shows the results from CV testing on cells that have been "warmed up" by cycling them at 0.2~C for 5 cycles, the same "warm up" used for galvanostatic charge-discharge testing.

During the cathodic scan of CV, measurements of the cells exhibit two related reduction peaks at around 2.3 and 2.0 V, which are assigned to the electrochemical reduction of sulfur into soluble polysulfides ( $S_8 \rightarrow \text{Li}_2S_x, \ x \geq 4$ , referred to as C I) and the subsequent reduction of long-chain polysulfides into insoluble  $\text{Li}_2S_2/\text{Li}_2S$  ( $\text{Li}_2S_x \rightarrow \text{Li}_2S_2/\text{Li}_2S, \ x \geq 4$ , referred to as C II), respectively. In the following anodic scan, the characteristic oxidation peaks correspond to the reverse conversion from insoluble  $\text{Li}_2S_2/\text{Li}_2S$  to the long-chain polysulfides ( $\text{Li}_2S_2/\text{Li}_2S \rightarrow \text{Li}_2S_x, \ x \geq 4$ ) and final oxidation into element sulfur ( $\text{Li}_2S_x \rightarrow S_8, \ x \geq 4$ , referred to as A).

Analyzing the peaks of the CV graphs shown in Fig. 5 (d) allows for analysis of the polarization potential of each of the cells. By finding the change in voltage between the cathodic peak near 2.0 V and the anodic peak near 2.5 V, the polarization potential can be obtained. A

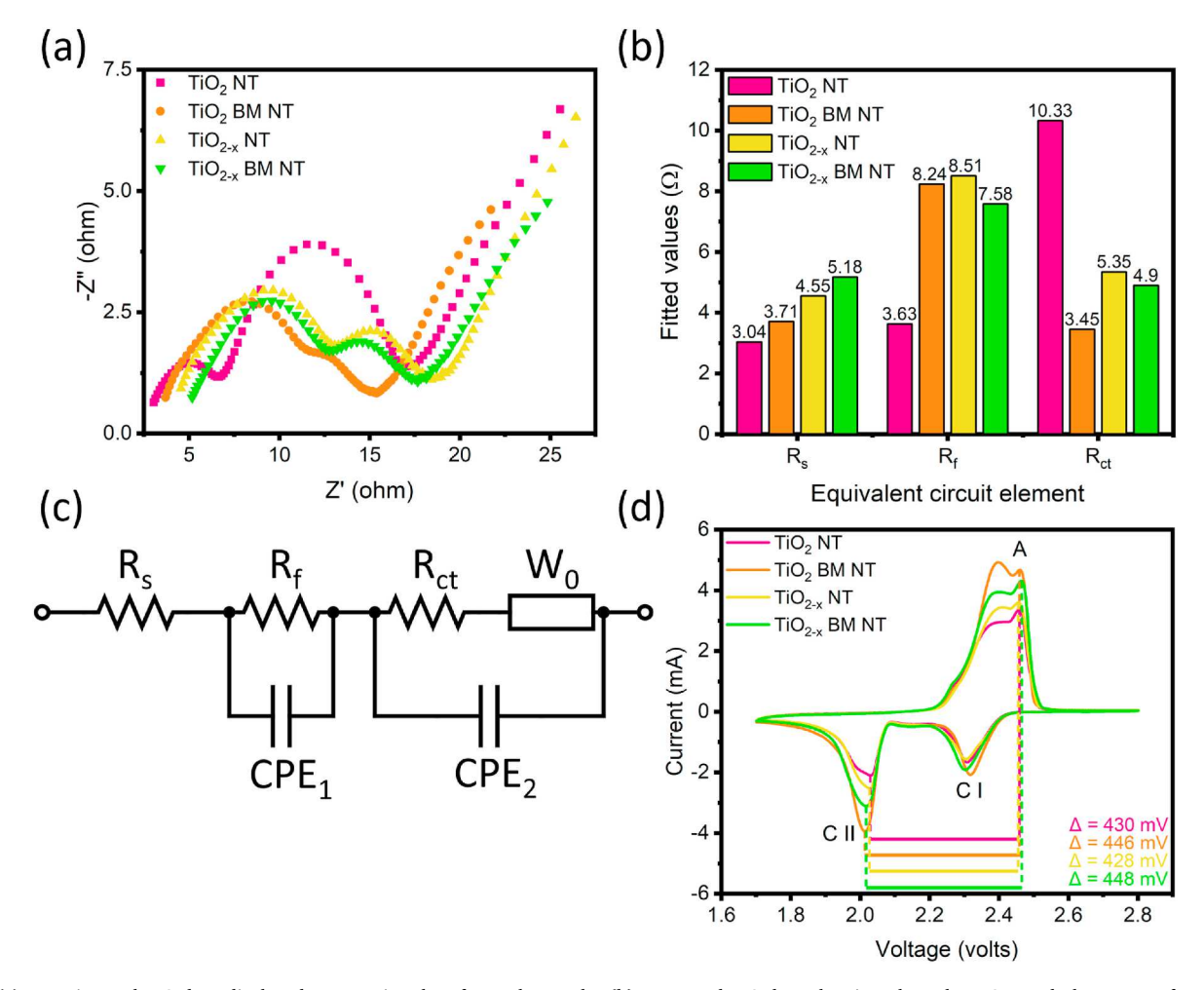


Fig. 5. (a) Experimental EIS data displayed as Nyquist plots for each sample, (b) Processed EIS data showing electrolyte, SEI and charge transfer resistance respectively for each cell, (c) Equivalent circuit diagram for the EIS testing, and (d) Experimental CV data for each sample.

polarization potential with a lower value indicates that the reaction has been catalyzed and is experiencing improved redox kinetics. Fig. 5 (d) shows a polarization potential of 430 mV for TiO $_2$  NTs@CC, 446 mV for TiO $_2$  BM NTs@CC, 428 mV for TiO $_2$ .x NTs@CC, and 448 mV for TiO $_2$ .x BM NTs@CC cells. The polarization potentials of all four cells were fairly similar, though there was a slight disparity between TiO $_2$  NTs based and TiO $_2$  BM NTs materials, with the slightly lower polarization potential of TiO $_2$  NTs based cathodes indicating that the material has a slight catalytic effect when compared to TiO $_2$  BM NTs. The lower polarization potential of the cells containing TiO $_2$  NT based materials in both pristine and reduced cases can be attributed to the polar metal oxide microstructures catalyzing the reduction of lithium polysulfides by acting as an electron bank and consequently increasing the speed of the reaction. The effect is more pronounced in cells containing TiO $_2$  NTs based materials due to the higher prevalence of NTs in these samples.

Fig. 5 (d) demonstrates maximum oxidation and reduction currents of 3.36 mA for peak A, 1.66 mA for peak CI, and 2.10 mA for peak CII for TiO2 NTs@CC cells, 4.68 mA for peak A, 2.08 mA for peak CI, and 3.95 mA for peak CII for TiO<sub>2</sub> BM NTs@CC cells, 3.60 mA for peak A, 1.56 mA for peak CI, and 2.52 mA for peak CII for TiO<sub>2-x</sub> NTs@CC cells, and 4.31 mA for peak A, 1.91 mA for peak CI, and 3.11 mA for peak CII for TiO<sub>2-x</sub> BM NTs@CC cells. Increased maximum current implies a higher rate of charge transfer by the cathode, corresponding to a higher conductivity of the cathode host material. In the case of the TiO2 NTs based cells, the cells employing TiO<sub>2-x</sub> NTs outperformed the cells employing TiO<sub>2</sub> NTs, owing to the increased conductivity from the chemically induced oxygen vacancies. This trend is not followed by the TiO2 BM NTs based cells, as the cells employing TiO<sub>2-x</sub> BM NTs are significantly outperformed by the TiO<sub>2</sub> BM NTs based cells. This result echoes the phenomenon observed in Fig. 2, indicating that chemical reduction is not compatible with the fragile structure of the TiO2 BM NTs material. The best overall performance is demonstrated by cells employing TiO2 BM NTs, indicating that increased and larger scale porosity has a large effect on the ability of the material to trap and reduce liquid lithium polysulfides.

Galvanostatic charge discharge cycling with a voltage window of 1.7–2.8 V was conducted to assess the capacity retention and overall stability of cells employing the  $\rm TiO_2$  NT host material over many cycles. Cyclic loading of cells at different charge rates (C), with 1 C being 1675 mAh g<sup>-1</sup>, was conducted via several different methods.

The maximum initial capacity and overall stability were assessed via a "step" test in which the C rate was changed every five cycles in the following order: 0.1, 0.2, 0.5, 1, 2, 3, 2, 1, 0.5, 0.2, 0.1 C. This test is shown in Fig. 6 (a-e) and summarized numerically in Table 1. This test is performed to determine how much the C rate influences the specific capacity of the cell and if high-rate cycling has a negative impact on specific capacity by allowing a comparison of cycling at low C rates before and after cycling at high C rates. Fig. 6 (a-c) show the best performance for each rate for each sample, while Fig. 6 (e) shows the full results of this test for  $\text{TiO}_2$  NTs,  $\text{TiO}_2$  BM NTs,  $\text{TiO}_2$ -x NTs,  $\text{TiO}_2$ -x BM NTs, and  $\text{TiO}_2$  BM. A  $\text{TiO}_2$  BM sample was used in this test to act as a baseline to measure the performance impact of each cathode host material. The  $\text{TiO}_2$  BM host material was only used as a reference for the steps test

Table 1
Initial discharge capacity of tested cells employing TiO<sub>2</sub> NTs, TiO<sub>2</sub> BM NTs, TiO<sub>2</sub>.

x NTs, and TiO<sub>2-x</sub> BM NTs respectively from Fig. 6(a–d).

Charge Rate	TiO <sub>2</sub> NTs	${ m TiO_2~BM}$ NTs	TiO <sub>2-x</sub> NTs	TiO <sub>2-x</sub> BM NTs	${ m TiO_2BM}$
С	${ m mAh~g^{-1}}$	$\rm mAh~g^{-1}$	$mAh g^{-1}$	mAh g <sup>-1</sup>	mAh g <sup>-1</sup>
0.1	1014	1205	1005	1054	848
0.2	898	1125	876	944	750
0.5	754	1024	806	848	677
1	689	927	738	770	616
2	614	843	571	679	552
3	551	768	354	616	495

because it is unable to maintain stability over long-term cycling. Each cathode host material demonstrated stable performance, with the best performance in terms of specific capacity being demonstrated by TiO2 BM NTs. As Fig. 6 (e) shows, specific capacities at each of the low C rates are unchanged after cycling. This loss of capacity at high C rates can be attributed to the kinetic nature of the lithium polysulfide electrochemical reaction, as the extent of the reaction in either direction is dependent on the amount of time provided for the lithium polysulfides to diffuse and react. TiO2 BM NTs outperformed TiO2-x BM NTs at both high and low C rates and maintained consistent performance after highrate cycling. TiO2 NTs significantly outperformed their chemically reduced counterparts at high C rates, however similar performance was observed at lower C rates. Each of the NTs based cathode materials significantly outperformed the TiO2 BM sample at low C rates, and all but the TiO<sub>2-x</sub> NTs sample outperformed the TiO<sub>2</sub> BM sample at high C rates.

Long-term stability tests were conducted at 3.0 C (Fig. 6 (f and g)). These tests showed very favorable results, shown in Table 2. Data collection beyond when the specific capacity of each sample falls below 95 mAh g<sup>-1</sup> is not displayed, as allows for an even comparison between cells and a focus on the number of cycles for which the cells can deliver a useful capacity. TiO<sub>2</sub> NTs demonstrated the best overall performance, boasting a capacity decay rate of only 0.004% per cycle for the first 300 cycles. TiO<sub>2</sub> BM NTs boasted a high initial capacity of 625 mAh g<sup>-1</sup>, however these cells also demonstrated a very low stability, with a capacity decay rate of 0.26% per cycle and only maintaining a useful capacity above 95 mAh g<sup>-1</sup> for 322 cycles. This difference in performance based on the synthesis method indicates a correlation between the mechanical robustness of the NT host material and the long-term stability. While the more porous TiO<sub>2</sub> BM NTs are able to achieve a higher initial capacity (as seen in Fig. 6 (e-g)), their fragile structure causes their capacitive performance to quickly fall off after extended cycling. While the more robust TiO2 NTs do not achieve the same capacity performance due to their less porous structure, they are able to achieve a much higher useable cycle life than TiO2 BM NTs, 676 as opposed to the 322 cycles it took for cells using TiO2 BM NTs to demonstrate a reversible capacity below 95 mAh g<sup>-1</sup>

Long-term stability tests conducted on chemically reduced samples,  ${\rm TiO}_{2\text{-x}}$  NTs and  ${\rm TiO}_{2\text{-x}}$  BM NTs respectively, demonstrated different results but indicated a similar trend.  ${\rm TiO}_{2\text{-x}}$  NTs demonstrated superior stability (decay rate of -0.68% per cycle over 300 cycles vs 0.022%) and higher initial capacity performance (383 mAh g $^{-1}$  vs 358 mAh g $^{-1}$ ) to  ${\rm TiO}_{2\text{-x}}$  BM NTs over 300 cycles, however, cells utilizing the  ${\rm TiO}_{2\text{-x}}$  NTs host failed at roughly 300 cycles. This trend indicates that, based on cycling data, the  ${\rm TiO}_{2\text{-x}}$  BM NTs were significantly damaged by chemical reduction, leading to a dramatic decrease in performance when compared to  ${\rm TiO}_2$  BM NTs.  ${\rm TiO}_{2\text{-x}}$  NTs, on the other hand, were able to hold up to the chemical reduction process as they demonstrated superior to  ${\rm TiO}_2$  NTs over 300 cycles.

The positive per cycle capacity "decay" experienced by the cell using the  ${\rm TiO}_{2.x}$  NTs cathode host shown in Table 2 is a result of the lithium polysulfide reaction reaching equilibrium after extended cycling. A maximum capacity is reached at roughly 100–150 cycles as more sulfur becomes activated and the cell stabilizes once its electrochemical equilibrium is reached. In tests run at low charge rates, this capacity gain can offset the capacity loss from the cyclic electrochemical wear on the cell, especially if the initial capacity is much lower than the maximum capacity reached at equilibrium. This combination of factors leads to a positive "decay", as the full capacity of the cell is not reached until enough sulfur is activated to reach the electrochemical equilibrium conditions of the cell [41–43].

As shown in Fig. S1, the battery with the  ${\rm TiO_{2-x}}$  NT electrode displayed an initial discharge capacity of 1134 mAh g $^{-1}$ . After 100 cycles, the capacity of the  ${\rm TiO_{2-x}}$  NT electrode remained at 1065 mAh g $^{-1}$ . However, the Li-S batteries with the  ${\rm TiO_2}$  NT electrode, the  ${\rm TiO_{2-x}}$  BM NT electrode, and the  ${\rm TiO_2}$  BM NT electrode demonstrated a slightly

Table 2
Values for initial, maximum, and final capacity for each sample for the cycling performed at 3.0 C in Fig. 6 (f and g).

Sample	Initial Capacity (mAh $g^{-1}$ )	Capacity at 300 Cycles (mAh $g^{-1}$ )	Final Capacity (mAh g <sup>-1</sup> )	Cycle Count	Per Cycle Capacity Decay (%) (300 cycles)	Per Cycle Capacity Decay (%)
TiO <sub>2</sub> NTs	429	424	95	676	0.004%	0.12%
TiO <sub>2</sub> BM NTs	625	133	94	322	0.26%	0.26%
TiO <sub>2-x</sub> NTs	383	459	~	294	-0.68%	~
TiO <sub>2-x</sub> BM	358	334	95	500	0.022%	0.15%
NTs						

poor initial discharge capacity of 1084 mAh g $^{-1}$ , 1030 mAh g $^{-1}$ , and 961 mAh g $^{-1}$  respectively. After 100 cycles, the capacity of the TiO $_2$  NT electrode, the TiO $_2$ -x BM NT electrode, and the TiO $_2$  BM NT electrode decayed to 997 mAh g $^{-1}$ , 939 mAh g $^{-1}$ , and 829 mAh g $^{-1}$  respectively. It can be seen that the initial discharge capacity and the final discharge capacity of the TiO $_2$ -x NT electrode was higher than the other three electrodes, confirming the superiority of polysulfides adsorption capability of TiO $_2$ -x NT. Defected TiO $_2$ -x NT with implanted oxygen vacancies can strengthen the polysulfides adsorption capability and improve the electronic conductivity. Additionally, it was reported that the normal TiO $_2$  structure can deform due to impact forces released by the collision of milling media [44], so the destruction of the tubular structures of the TiO $_2$  nanotubes can be caused by high-energy ball milling and affect their performance.

Since the  $TiO_{2-X}$  NT electrode demonstrated the most favorable electrochemical performance under low sulfur loading among all the samples, furthermore, taking the practical commercialization into account, the electrochemical measurement for the  $TiO_{2-X}$  NT electrode with high areal sulfur loading (5 mg cm $^{-2}$ ) was carried out (Fig. S2). The  $TiO_{2-X}$  NT cell displayed an initial capacity of 766 mAh g $^{-1}$  and retained at 718 mAh g $^{-1}$  after 50 cycles. The cycling performance under high sulfur loading is one of the most powerful pieces of evidence for the  $TiO_{2-X}$  NT as a promising sulfur host. It is clear that  $TiO_{2-X}$  NT can effectively trap soluble polysulfides via polar-polar chemical interactions [45–47]. The outstanding cycling stability under high sulfur loading demonstrate the  $TiO_{2-X}$  NT cell is full of promise, becoming an outstanding candidate for practical applications.

# 3.4. Characterization after cycling

To qualitatively and quantitatively determine the impact of the  $\rm TiO_2$  NTs based cathode host materials on PSE, cells cycled using a cathode with the  $\rm TiO_2$  NTs host material, the host material which demonstrated the most stable long-term performance, were compared to cells cycled using unmodified  $\rm TiO_2$  as a cathode host material. This comparison was done twice, once with cells using cathodes of both types cycled under identical conditions to analyze the extent of PSE on the separator material qualitatively, and once using cells of both types cycled at as high of a rate and as for long of a duration as each cell was capable of to determine the impact of PSE on the surface of the lithium metal anode both qualitatively and quantitatively.

After cycling, the extent of polysulfide trapping, and conversely the extent of alleviation of PSE, can be determined qualitatively by disassembling used cells and examining the separator material. When unused, the separator is white, picking up color from molecules retained in the electrolyte. Sulfur appears yellow under visible light, and thus the amount of sulfur that was not retained by the host material can be assessed by assessing color. This is shown in Fig. 7. Note that black particles and very dark areas are due to carbon cloth pulverization during the cell's sealing process and has no effect on performance. Fig. 7 (a) displays the separator material from a cell cycled 300 times at 1.0 C with the TiO<sub>2</sub> NTs@CC cathode. Fig. 7 (b) displays the separator material from a cell cycled 100 times at 1.0 C with a TiO2@CC cathode. This material was chosen as a reference for poor performance due to the fact that raw TiO2 does not improve cell performance but allows cathodes to be made in an identical fashion. Despite undergoing 3 times as much cycling as the other sample, samples containing TiO2 NT display

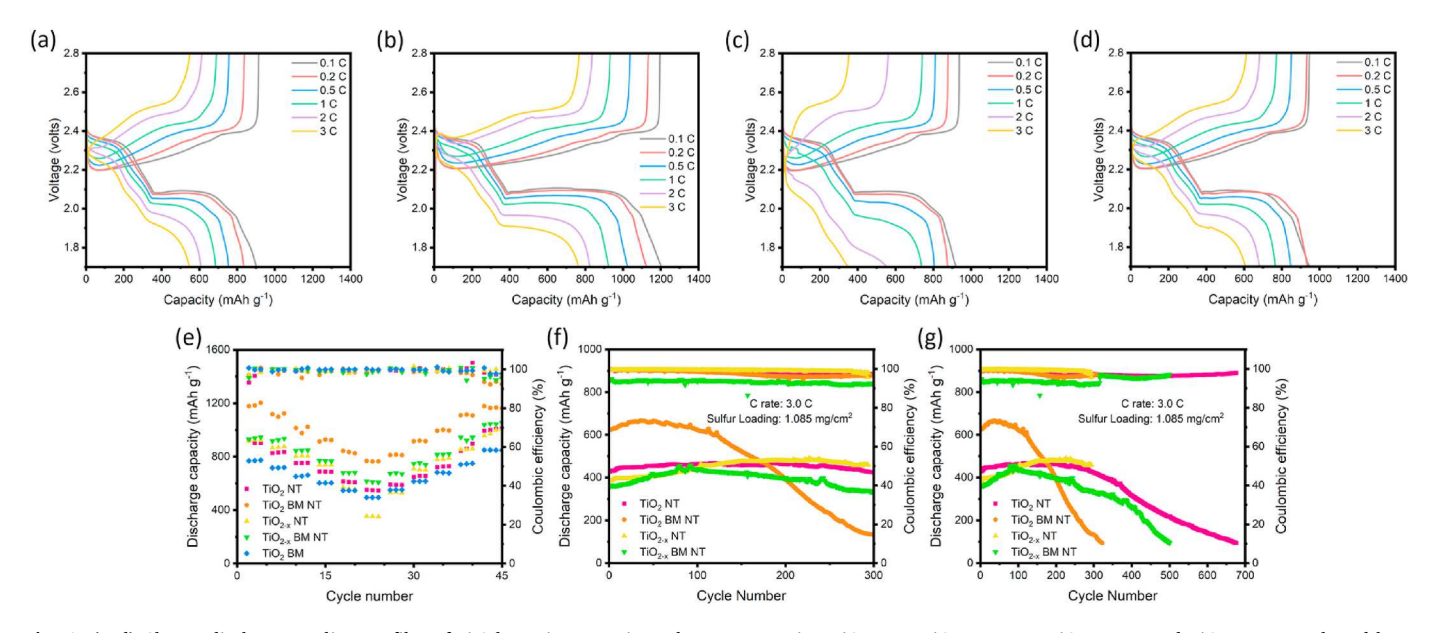


**Fig. 6.** (a–d) Charge-discharge cycling profiles of Li-S batteries at various charge rates using  $TiO_2$  NTs,  $TiO_2$  BM NTs,  $TiO_{2\cdot x}$  NTs, and  $TiO_{2\cdot x}$  BM NTs based host materials on carbon cloth as cathodes respectively. (e) displays of "steps" tests conducted on Li-S batteries between charge rates of 0.1 and 3.0 C for  $TiO_2$  NTs,  $TiO_2$  BM NTs,  $TiO_{2\cdot x}$  NTs,  $TiO_{2\cdot x}$  NTs,  $TiO_{2\cdot x}$  BM NTs, and  $TiO_2$  BM based host materials. (f and g) display of long cycling tests conducted at 3.0 C, showing the first 300 cycles and the performance of each cell until failure or a capacity of less than 95 mAh g<sup>-1</sup> respectively.

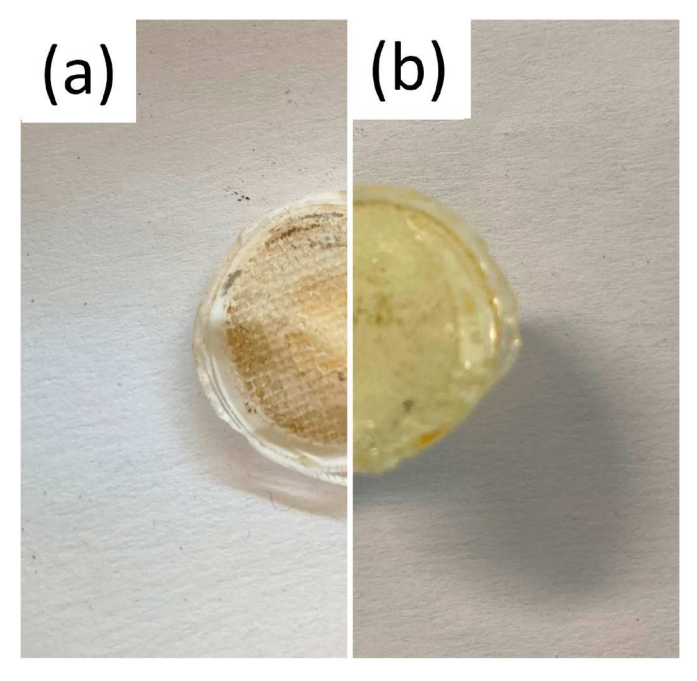


Fig. 7. (a) Image of the separator of a cell employing TiO2 NT after 300 cycles at 1.0 C and (b) image of the separator of a cell employing TiO2 after 100 cycles at 1.0 C.

superior polysulfide retention due to their lighter coloration. Both images were taken immediately after the disassembly of the cells and show the coloration of the electrolyte they are saturated with.

The extent of elimination of PSE can also be measured by analyzing the contact surface of the lithium anode. PSE causes the surface to dissolve and deposit unevenly, as it causes the passivation of parts of the anode, creating "dead" zones that can no longer interact with the electrolyte. Fig. 8 (a and c) show the SEM images of the contact surface of a lithium anode after 300 cycles at 1 C with a TiO2@CC cathode with large-scale defects labeled. Fig. 8 (b and d) show the SEM images of the contact surface of a lithium anode after 1000 cycles at 3 C with TiO<sub>2</sub> NTs@CC as a cathode. This disparity in cycling conditions is due to the fact that the TiO<sub>2</sub>@CC cathode was not stable enough to support cycling at very high rates or over long durations. Despite being run at a charge rate three times higher and for more than three times as long, the contact surface from the cell employing TiO2 NTs demonstrates a smooth surface, indicating that no regions are "dead", implying PSE has been minimized. Fig. 8 (a and c) demonstrate the impact of PSE, showing the dendrites and porosity formed from uneven dissolution and deposition of the lithium ions back onto the surface. This is supported by energy dispersive X-ray analysis (EDAX) of both anodes, shown in Fig. 8 (e and f). EDAX allows for analysis of the surface composition of a material by indicating what elements are present on the surface and their relative concentrations from surface area fraction. In this case, it is used to identify zones of the anode where sulfur is present, as it indicates the dead zones on the surface where passivation films have been formed. A higher surface area fraction of sulfur indicates that more of the surface of the lithium anode's contact surface has been passivated via a film of solid lithium sulfide, implying a more severe impact from PSE. EDAX analysis revealed the presence of 9.6 wt % sulfur on the surface of the anode of the cell using the unrefined TiO2 host cathode and the presence of 6.6 wt % sulfur on the surface of the anode of the cell using the TiO<sub>2</sub> NTs cathode. These results show that the anode from the cell employing TiO<sub>2</sub> NTs has a lower presence of sulfur on its surface despite being cycled for more than three times as many cycles at an intensity 3 times greater. This indicates that the presence of TiO2 NTs in the cathode has a dramatic impact on PSE, able to prevent a significant amount of polysulfide diffusion via adsorption.

#### 3.5. Discussion

The effectiveness of TiO2 NTs based host materials as lithium polysulfide hosts in Li-S batteries can be attributed to their complex geometry and polar nature. The synergy of these two properties creates a host material that is able to both physically and chemically confine liquid lithium polysulfides, effectively immobilizing them during the intermediate liquid phases of electrochemical reduction and severely limiting the impact of PSE. Fig. 9 shows SEM images demonstrating the complex structure of the TiO2 NTs, with both interior and exterior portions able to make contact with the electrolyte solution and interact with ions in the solution. The conductivity and polar nature of the TiO2 NTs based host materials were found to be further improved by chemical reduction, however the initial TiO2 NTs material had to be mechanically robust enough to withstand chemical treatment without losing the NT structures from its surface. Of the four TiO2 NTs derived materials, the best overall performance in terms of capacity and performance was attributed to the TiO<sub>2</sub> BM NTs based cathode host materials, while the TiO<sub>2-x</sub> NTs based cathode host demonstrated the best overall stability. The TiO<sub>2</sub> BM NTs sample was too mechanically fragile for the chemical reduction process, and additionally was unable to stand up to cycling over extended periods of time due to the same factor. Cells employing the TiO<sub>2</sub> BM NTs cathode host achieved a maximum initial specific capacity of 1204.72 mAh g<sup>-1</sup> at 0.1 C and a maximum initial specific capacity of 767.69 mAh g<sup>-1</sup> at 3.0 C, however were only able to provide a specific capacity greater than 95 mAh g<sup>-1</sup> for 322 cycles at 3.0 C, with a moderate capacity decay rate of 0.26% per cycle. Similarly, cells employing the TiO2-x BM NTs cathode also demonstrated high initial specific capacities, showing a maximum initial specific capacity of 1054.35 mAh  $g^{-1}$  at 0.1 C and a maximum initial specific capacity of 616.22 mAh  $g^{-1}$ at 3.0 C. Despite the decreased initial specific capacities at every charge rate, the  $TiO_{2-x}$  BM NTs cathode was able to cycle 500 times before falling below a capacity of 95 mAh g<sup>-1</sup>, demonstrating an impressively low capacity decay rate of 0.022% per cycle for the first 300 cycles and an overall decay rate of 0.15% per cycle. The more stable TiO2 NTs cathode was able to maintain a specific capacity above 95 mAh g<sup>-1</sup> for 676 cycles, boasting an impressively low capacity decay rate of 0.004% per cycle for the first 300 cycles, and 0.12% per cycle overall. Cells using this cathode host material achieved a maximum initial specific capacity of 1013.7 mAh  $\mathrm{g}^{-1}$  at 0.1 C and a maximum initial specific capacity of 551.41 mAh  $g^{-1}$  at 3.0 C. The TiO<sub>2-x</sub> NTs cathode demonstrated the best stability in the first 300 cycles with a capacity decay rate of -0.68% per cycle, however this cathode was only able to cycle for a maximum of 294 cycles before becoming unstable. Cells using this cathode material demonstrated a maximum initial specific capacity of 1054.35 mAh g<sup>-1</sup> at 0.1 C and a maximum initial specific capacity of 616.22 mAh g<sup>-1</sup> 3.0C. TiO2 NTs based cathodes and TiO2-x NTs based cathodes both demonstrated impressive stability in the first 300 cycles, however the TiO<sub>2-x</sub> NTs cathodes suffered significantly decreased performance at high charge rates. All four materials demonstrated a severe performance drop off after 300-400 cycles, with this effect being especially prominent with the more mechanically fragile cathode host materials such as TiO<sub>2</sub> BM NTs.

This examination gave clear results indicating the superior ability of TiO2 NT based materials to alleviate PSE, as all cells containing NTs were able to demonstrate impressive capacity and stability performance over 300 cycles. A clear impact of initial particle size for nanotube synthesis on cell performance was observed, with the use of ball-milled particles resulting in a more open nanotube structure which was able to demonstrate higher capacities than its more closed counterpart, although for a shorter cyclic duration. The introduction of oxygen vacancies onto the nanotube structures via chemical reduction was also tested, revealing a positive impact on the conductivity of samples mechanically robust enough to withstand it. The advantage and disadvantage of TiO2 NTs, compared With TiO2 quantum dots, TiO2 nanoparticles, TiO2 hollow spheres, TiO2 nanowires and TiO2

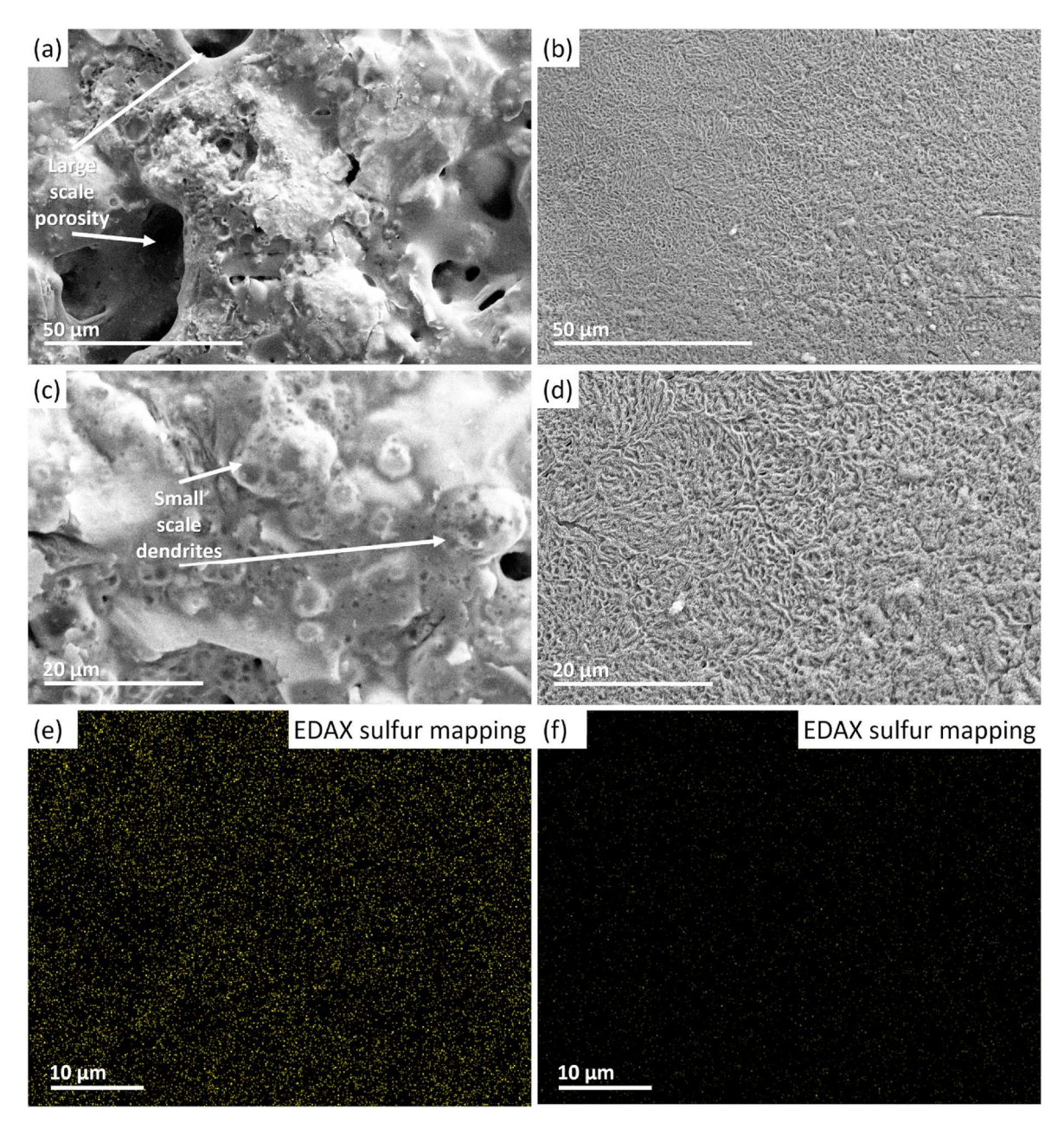


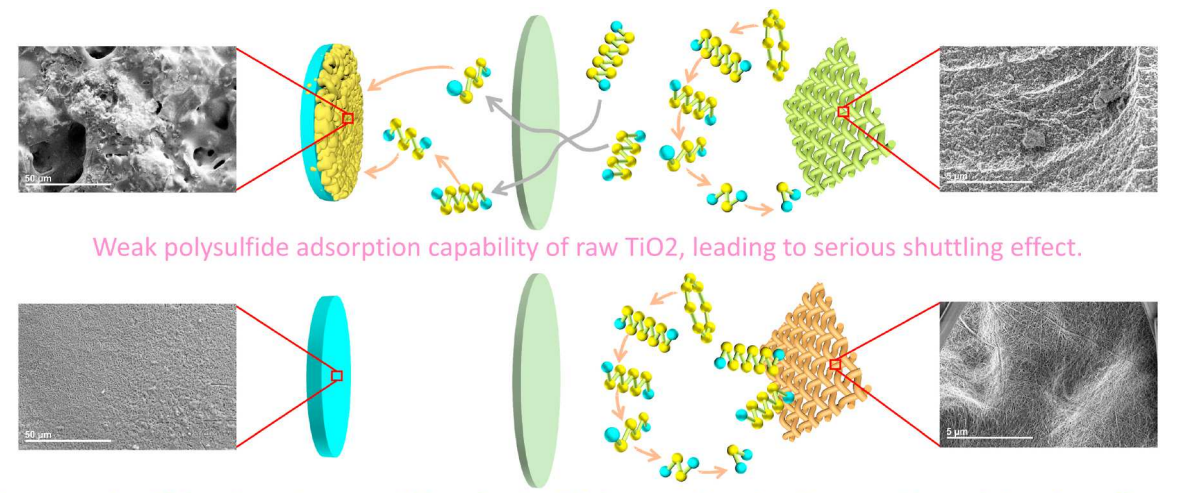
Fig. 8. SEM images of the contact surface of the lithium anode for (a) a cell that employed  $TiO_2$  at 1000x, (b) a cell that employed  $TiO_2$  NTs at 1000x, (c) a cell that employed  $TiO_2$  at 2000x, (d) a cell that employed  $TiO_2$  NT at 2000x. EDX scans at 2000x magnification showing the presence of sulfur in yellow for (e) a cell that employed  $TiO_2$  and (f) a cell that employed  $TiO_2$  NTs.

nanosheets for the applications in Li-S battery are shown in supporting information (Table S2).

# 4. Conclusion

 ${
m TiO_2}$  NTs were prepared via a simple hydrothermal template synthesis method and employed as a polar cathode host material for Li-S batteries. Samples were prepared from unmodified and ball milled rutile  ${
m TiO_2}$  powders, and subsequently chemically reduced to create oxygen vacancies to synthesize four distinct cathode host materials,  ${
m TiO_2}$  NTs,  ${
m TiO_2}$  BM NTs,  ${
m TiO_{2-x}}$  NTs, and  ${
m TiO_{2-x}}$  BM NTs respectively. SEM and TEM analysis techniques revealed the structures as hollow tubes, with exposed structures belonging primarily to the (2 0 0) crystal plane of anatase phase  ${
m TiO_2}$ . SEM analysis indicated a large difference in the topography and geometry of the  ${
m TiO_2}$  NTs and  ${
m TiO_2}$  BM NTs samples, with the  ${
m TiO_2}$  NTs demonstrating a much more mechanically robust

structure due to the larger initial particle size causing the NTs to grow as a "mat" on the surface of the particles, and the TiO2 BM NTs demonstrating a much more porous and open structure due to the smaller initial particle size causing the NTs to grow as a "web" between the particles. The more mechanically robust TiO2 NTs and TiO2-x NTs particles showed better overall performance, as the delicate nature of the TiO2 BM NTs based materials caused the NTs structure to be destroyed by long-term cycling and chemical reduction. While the TiO2 BM NTs showed the best performance in terms of capacity, achieving an initial specific capacity of 1204.72 mAh g $^{-1}$  at 0.1 C and 767.69 mAh g $^{-1}$  at 3 C, they lacked considerable stability, only able to provide a specific capacity above 95 mAh g<sup>-1</sup> for 322 cycles at 3 C and demonstrating a high decay rate of 0.26% per cycle.  $\rm TiO_2\,NTs$  and  $\rm TiO_{2\text{-}x}\,NTs$  were able to deliver lower initial specific capacities, 1013.7 and 1005.24 mAh  $\mathrm{g}^{-1}$  at 0.1 C and 551.41 and 616.22 mAh g<sup>-1</sup> at 3 C respectively, and extremely low decay rates over the first 300 cycles, 0.004% and -0.68% per cycle



Strong polysulfide adsorption capability of polar TiO2 nanotubes, leading to mitigated shuttling effect.

Fig. 9. Schematic demonstrating how TiO2 NTs based cathode host materials can help to mitigate PSE.

respectively. The TiO<sub>2</sub> NTs were able to cycle above 95 mAh g<sup>-1</sup> for 676 cycles, whereas the TiO2-x NTs only achieved 294 stable cycles. The negative capacity decay rate of the TiO<sub>2-x</sub> NTs indicates that the cell was still reaching equilibrium around 300 cycles, indicating very stable performance for cells using this cathode that cycle stability. Overall, this work determined that Li-S battery cathode host materials must demonstrate a high level of mechanical robustness to endure long cycling, as evidenced by the superior long-term performance of the TiO<sub>2</sub> NTs host material. The chemical reduction was shown to be a suitable method to introduce oxygen deficiency in TiO2 nanostructures, as evidenced by the superior electrochemical performance and lower internal resistance of cells using the TiO2-x NTs host material. This work explores the use of polar host materials which chemically and physically bind and confine liquid lithium polysulfides and alleviate the polysulfide shuttling effect, indicating the direction for further investigation, and incrementing toward the feasibility of commercial Li-S batteries.

# CRediT authorship contribution statement

**Zephyr Barlow:** Investigation, Methodology, Formal analysis, Writing – original draft, Writing – review & editing. **Zhen Wei:** Formal analysis, Writing – review & editing. **Ruigang Wang:** Conceptualization, Supervision, Writing – review & editing, Funding acquisition.

# Declaration of competing interest

The authors declare that they have no known competing financial interests or personal relationships that could have appeared to influence the work reported in this paper.

# Data availability

No data was used for the research described in the article.

#### Acknowledgment

This work is supported by the National Science Foundation (CBET-2118784 and TI-2147564). This project also receives partial financial support from Alabama Transportation Institute and Alabama Water Institute. The use of electron microscopy facilities at the Alabama Analytical Research Center (AARC), The University of Alabama, is gratefully acknowledged.

# Appendix A. Supplementary data

Supplementary data to this article can be found online at https://doi.org/10.1016/j.matchemphys.2023.128316.

#### References

- J. He, A. Manthiram, A review on the status and challenges of electrocatalysts in lithium-sulfur batteries, Energy Storage Mater. 20 (2019) 55–70.
- [2] A. Manthiram, Y. Fu, S.H. Chung, C. Zu, Y.S. Su, Rechargeable lithium-sulfur batteries, Chem. Rev. 114 (2014) 11751–11787.
- [3] Z. Wei, R. Wang, Chemically etched CeO2-x nanorods with abundant surface defects as effective cathode additive for trapping lithium polysulfides in Li-S batteries, J. Colloid Interface Sci. 615 (2022) 527–542.
- [4] S. Azam, Z. Wei, R. Wang, Adsorption-catalysis design with cerium oxide nanorods supported nickel-cobalt-oxide with multifunctional reaction interfaces for anchoring polysulfides and accelerating redox reactions in lithium sulfur battery, J. Colloid Interface Sci. 635 (2022) 466–480.
- [5] S.-J. Kwon, S.-E. Lee, J.-H. Lim, J. Choi, J. Kim, Performance and life degradation characteristics analysis of NCM LIB for BESS, Electronics 7 (2018) 406.
- [6] U.S.G. Survey, Mineral Commodity Summaries 2023, U.S. Geological Survey, 2023.
- [7] S. Fahad, Z. Wei, A. Kushima, In-situ TEM observation of fast and stable reaction of lithium polysulfide infiltrated carbon composite and its application as a lithium sulfur battery electrode for improved cycle lifetime, J. Power Sources 506 (2021) 230175.
- [8] S. Azam, Z. Wei, R. Wang, Cerium oxide nanorods anchored on carbon nanofibers derived from cellulose paper as effective interlayer for lithium sulfur battery, J. Colloid Interface Sci. 615 (2022) 417–431.
- [9] H. Kim, K.J. Min, S. Bang, J.Y. Hwang, J.H. Kim, C.S. Yoon, Y.K. Sun, Long-lasting, Reinforced Electrical Networking in a High-loading Li2S Cathode for Highperformance Lithium–Sulfur Batteries, Carbon Energy, 2023.
- [10] F. Han, J. Yue, X. Fan, T. Gao, C. Luo, Z. Ma, L. Suo, C. Wang, High-performance all-solid-state lithium-sulfur battery enabled by a mixed-conductive Li2S nanocomposite, Nano Lett. 16 (2016) 4521–4527.
- [11] H. Li, Y. Li, L. Zhang, Designing principles of advanced sulfur cathodes toward practical lithium-sulfur batteries, SusMat 2 (2022) 34–64.
- [12] A. Ali, S. Sarwar, D.R. Pollard, Z. Wei, R. Wang, X. Zhang, A.J. Adamczyk, Systematic mapping of electrocatalytic descriptors for hybrid and non-hybrid molybdenum dichalcogenides with graphene support for cathodic hydrogen generation, J. Phys. Chem. C 126 (2022) 17011–17024.
- [13] W. Yao, C. Tian, C. Yang, J. Xu, Y. Meng, I. Manke, N. Chen, Z. Wu, L. Zhan, Y. Wang, P-Doped NiTe2 with Te-vacancies in lithium-sulfur batteries prevents shuttling and promotes polysulfide conversion, Adv. Mater. 34 (2022), 2106370.
- [14] Z. Wei, Lithium Polysulfide Battery with Improved Capacity and Cycle Performance Using Carbon Black Coated Free-Standing Carbon Cloth, University of Central Florida, 2019.
- [15] L. Zhou, D.L. Danilov, R.A. Eichel, P.H.L. Notten, Host materials anchoring polysulfides in Li–S batteries reviewed, Adv. Energy Mater. 11 (2020), 2001304.
- [16] S. Yao, H. Tang, M. Liu, L. Chen, M. Jing, X. Shen, T. Li, J. Tan, TiO2 nanoparticles incorporation in carbon nanofiber as a multi-functional interlayer toward ultralong cycle-life lithium-sulfur batteries, J. Alloys Compd. 788 (2019) 639–648.
- [17] J. Li, Y. Qu, C. Chen, X. Zhang, M. Shao, Theoretical investigation on lithium polysulfide adsorption and conversion for high-performance Li-S batteries, Nanoscale 13 (2021) 15–35.
- [18] Y. Yan, T. Lei, Y. Jiao, C. Wu, J. Xiong, TiO2 nanowire array as a polar absorber for high-performance lithium-sulfur batteries, Electrochim. Acta 264 (2018) 20–25.

- [19] N. Li, F. Chen, X. Chen, Z. Chen, Y. Qi, X. Li, X. Sun, A bipolar modified separator using TiO2 nanosheets anchored on N-doped carbon scaffold for high-performance Li–S batteries, J. Mater. Sci. Technol. 55 (2020) 152–158.
- [20] X. Shan, Z. Guo, X. Zhang, J. Yang, L. Duan, Mesoporous TiO2 nanofiber as highly efficient sulfur host for advanced lithium-sulfur batteries, Chin. J. Mech. Eng. 32 (2019) 1–6.
- [21] J. Yang, D. Ma, Y. Li, P. Zhang, H. Mi, L. Deng, L. Sun, X. Ren, Atomic layer deposition of amorphous oxygen-deficient TiO2-x on carbon nanotubes as cathode materials for lithium-air batteries, J. Power Sources 360 (2017) 215–220.
- [22] E.H.M. Salhabi, J. Zhao, J. Wang, M. Yang, B. Wang, D. Wang, Hollow multishelled structural TiO(2-x) with multiple spatial confinement for long-life lithiumsulfur batteries, Angew Chem. Int. Ed. Engl. 58 (2019) 9078–9082.
- [23] J. Huang, S. Dong, Hierarchically porous titanium dioxide as efficient sulfur host for advanced lithium-sulfur batteries, Ionics 28 (2022) 2775–2779.
- [24] Y. Cai, Z. Yan, S. Shi, L. Zhang, T. Zhang, M. Yang, L. Bai, H. Fu, X.-S. Yang, Z. Li, Z.-D. Huang, Titanium oxide nanowire clots with two-phase composition as multieffect sulfur reservoirs for lithium-sulfur batteries, Scripta Mater. 202 (2021) 112020
- [25] G.D. Park, J.K. Lee, Y.C. Kang, Electrochemical properties of sulfur-carbon hollow nanospheres with varied polar titanium oxide layer location for lithium-sulfur batteries, Int. J. Energy Res. 46 (2022) 9071–9079.
- [26] M. Liu, S. Jhulki, A. Magasinski, P.F. Wang, G. Yushin, Porous TiO(2-x)/C nanofibers with axially aligned tunnel pores as effective sulfur hosts for stabilized lithium-sulfur batteries, ACS Appl. Mater. Interfaces 14 (2022) 54725–54735.
- [27] M.G. Choi, Y.-G. Lee, S.-W. Song, K.M. Kim, Lithium-ion battery anode properties of TiO2 nanotubes prepared by the hydrothermal synthesis of mixed (anatase and rutile) particles, Electrochim. Acta 55 (2010) 5975–5983.
- [28] T. Appadurai, C.M. Subramaniyam, R. Kuppusamy, S. Karazhanov, B. Subramanian, Electrochemical performance of nitrogen-doped TiO2 nanotubes as electrode material for supercapacitor and Li-ion battery, Molecules 24 (2019) 2952.
- [29] Y. Chen, W. Tang, J. Ma, B. Ge, X. Wang, Y. Wang, P. Ren, R. Liu, Nickel-decorated TiO2 nanotube arrays as a self-supporting cathode for lithium-sulfur batteries, Front. Mater. Sci. 14 (2020) 266–274.
- [30] N. Liu, L. Wang, Y. Zhao, T. Tan, Y. Zhang, Hierarchically porous TiO2 matrix encapsulated sulfur and polysulfides for high performance lithium/sulfur batteries, J. Alloys Compd. 769 (2018) 678–685.
- [31] Z. Wei Seh, W. Li, J.J. Cha, G. Zheng, Y. Yang, M.T. McDowell, P.C. Hsu, Y. Cui, Sulphur-TiO2 yolk-shell nanoarchitecture with internal void space for long-cycle lithium-sulphur batteries, Nat. Commun. 4 (2013) 1331.
- [32] A. Sabbaghi, C.H. Wong, X. Hu, F.L.Y. Lam, Titanium dioxide nanotube arrays (TNTAs) as an effective electrocatalyst interlayer for sustainable high-energy density lithium-sulfur batteries, J. Alloys Compd. 899 (2022).
- [33] V. Sama, Synthesis and Characterization of CexTi1-xO2 Nanostructures, Chemistry, Youngstown State University, 2013, p. 115.

- [34] Y. Wang, Z. Liu, R. Wang, NaBH4 surface modification on CeO2 nanorods supported transition-metal catalysts for low temperature CO oxidation, ChemCatChem 12 (2020) 4304–4316.
- [35] Z.-Y. Yuan, B.-L. Su, Titanium oxide nanotubes, nanofibers and nanowires, Colloids Surf. A Physicochem. Eng. Asp. 241 (2004) 173–183.
- [36] G.H. Du, Q. Chen, R.C. Che, Preparation and structure analysis of titanium oxide nanotubes, Appl. Phys. Lett. 79 (2001) 3702–3704.
- [37] D. Wang, F. Zhou, Y. Liu, W. Liu, Synthesis and characterization of anatase TiO2 nanotubes with uniform diameter from titanium powder, Mater. Lett. 62 (2008) 1819–1822.
- [38] M. Chu, Y. Tang, N. Rong, X. Cui, F. Liu, Y. Li, C. Zhang, P. Xiao, Y. Zhang, Hydrothermal synthesis, and tailoring the growth of Ti-supported TiO2 nanotubes with thick tube walls, Mater. Des. 97 (2016) 257–267.
- [39] D.S. Wu, F. Shi, G. Zhou, C. Zu, C. Liu, K. Liu, Y. Liu, J. Wang, Y. Peng, Y. Cui, Quantitative investigation of polysulfide adsorption capability of candidate materials for Li-S batteries, Energy Storage Mater. 13 (2018) 241–246.
- [40] S. Yang, X. Wang, X. Yang, Y. Bai, Z. Liu, H. Shu, Q. Wei, Determination of the chemical diffusion coefficient of lithium ions in spherical Li[Ni0.5Mn0.3Co0.2]O2, Electrochim. Acta 66 (2012) 88–93.
- [41] J. Jiang, J. Zhu, W. Ai, X. Wang, Y. Wang, C. Zou, W. Huang, T. Yu, Encapsulation of sulfur with thin-layered nickel-based hydroxides for long-cyclic lithium-sulfur cells, Nat. Commun. 6 (2015) 8622.
- [42] T. Ma, F. Zhou, T.W. Zhang, H.B. Yao, T.Y. Su, Z.L. Yu, Y. Li, L.L. Lu, S.H. Yu, Large-scale syntheses of zinc sulfide-(diethylenetriamine)(0.5) hybrids as precursors for sulfur nanocomposite cathodes, Angew Chem. Int. Ed. Engl. 56 (2017) 11836–11840.
- [43] X. Wang, Y. Qian, L. Wang, H. Yang, H. Li, Y. Zhao, T. Liu, Sulfurized polyacrylonitrile cathodes with high compatibility in both ether and carbonate electrolytes for ultrastable lithium-sulfur batteries, Adv. Funct. Mater. 29 (2019), 1902929.
- [44] V.N. Kudiyarov, R.R. Elman, N.E. Kurdyumov, The effect of high-energy ball milling conditions on microstructure and hydrogen desorption properties of magnesium hydride and single-walled carbon nanotubes, Metals 11 (2021) 1409.
- [45] Z. Wei, J. Li, Y. Wang, R. Wang, High-performance Li-S batteries enabled by polysulfide-infiltrated free-standing 3D carbon cloth with CeO2 nanorods decoration, Electrochim. Acta 388 (2021) 138645.
- [46] Z. Wei, J. Li, R. Wang, Surface engineered polar CeO2-based cathode host materials for immobilizing lithium polysulfides in High-performance Li-S batteries, Appl. Surf. Sci. 580 (2022) 152237.
- [47] Z. Wei, S. Sarwar, S. Azam, M.R. Ahasan, M. Voyda, X. Zhang, R. Wang, Ultrafast microwave synthesis of MoTe2@ graphene composites accelerating polysulfide conversion and promoting Li2S nucleation for high-performance Li-S batteries, J. Colloid Interface Sci. 635 (2023) 391–405.